


Preparation of $\text{Al}_2\text{O}_3\text{--Cr}_2\text{O}_3$ Solid Solutions as Buoyancy Markers and Their High Pressure Synchrotron X-ray Diffraction AnalysisHANSHU LIU,¹ LIANG LI,² BENXIAN LI,^{1,3}  XIAOFENG WANG,⁴ LIANG SUN,⁵ BIN YANG,⁶ XUDONG ZHAO,⁴ KEXIN FEI,¹
and XIAOYANG LIU^{1,4}HPSTAR
1391-2022

Abstract—Understanding the density of silicate melts under high pressures is of great significance for establishing the differentiation and dynamic modeling of materials in the interior of the Earth. The sink/float method is widely used in the density measurement of silicate melts under high pressures. However, there are significant limitations in using natural minerals as buoyancy markers in this method. In this study, the $\text{Al}_2\text{O}_3\text{--Cr}_2\text{O}_3$ solid solution, which is a buoyancy marker, was prepared using the optical floating zone melting method. The crystalline structures of $\text{Al}_2\text{O}_3\text{--Cr}_2\text{O}_3$ solid solutions with different Cr_2O_3 contents at ambient pressure were studied. It was found that lattice parameters a and c increase linearly with the increasing Cr_2O_3 content, but the doping with Cr^{3+} ions leads to a more severe lattice strain in the c -axis direction. As the Cr_2O_3 content increases, the diffraction angle of the diffraction peak decreases linearly. In addition, it was found that the relationship between the theoretical density of each solid solution and its Cr_2O_3 content can be fitted using a second-order polynomial. Al95Cr05, Al90Cr10, and Al30Cr70 were analyzed using synchrotron radiation X-ray diffraction analysis under different pressures in order to study the stability and compressibility of the $\text{Al}_2\text{O}_3\text{--Cr}_2\text{O}_3$ solid solutions under high pressure. The results show that the cell parameters of the three solid solutions vary with pressure. The bulk elastic moduli of these three solid solutions were obtained, which provides experimental data for the design and preparation of different buoyancy markers in the future.

Keywords: High pressure, synchrotron, $\text{Al}_2\text{O}_3\text{--Cr}_2\text{O}_3$ solid solution, X-ray diffraction.

1. Introduction

Silicate melt is an important carrier of material and energy in the Earth. It plays a key role in the formation and evolution of the Earth, and it is also closely related to the formation of many metal deposits (Bouhifd et al., 2016; Eakins-Tanton, 2012; Mysen, 2018). In the early formation stage of the Earth, large-scale melting and melting-crystallization processes may have occurred in the Earth's interior under extremely high-temperature conditions (Guillaume et al., 2018). The density differences between the materials promoted the formation of the Earth and its spherical structure (Agee, 2008; Lagos et al., 2008). The density of silicate melts controlled the formation of the mantle and crust (Solomatova & Caracas, 2021). Experimental studies of metal/silicate zoning show that there may be a magma ocean in the Earth (Chabot et al., 2005; Kuwahara et al., 2017; Li & Agee, 2001). During the Earth's rapid growth and material differentiation, minerals were constantly being separated from the magma. The densities of the melt and its coexisting crystals not only controlled the separation of the liquid and solids, but they also controlled the properties of the early Earth and its internal structure to a great extent, such as the transport properties of the materials (Agee, 2008; Lagos et al., 2008). Magmatism makes the interior of the Earth and earth-like planets undergo material differentiation and energy transmission under the planet's gravitational field, and it forms the ring structure of the modern Earth and earth-like planets (Agee, 2008; Courtial et al., 1997; Matsukage et al., 2005; Suzuki & Ohtani, 2003). To understand and model magmatic processes, knowledge of the

¹ College of Earth Sciences, Jilin University, Changchun 130061, China. E-mail: lbxian@jlu.edu.cn; liuxy@jlu.edu.cn

² College of Physics, Jilin University, Changchun 130012, China.

³ Key Laboratory of Mineral Resources Evaluation in Northeast Asia, Ministry of Natural Resources of the People's Republic of China, Changchun 130061, China.

⁴ State Key Laboratory of Inorganic Synthesis and Preparative Chemistry, Jilin University, Changchun 130012, China.

⁵ Logging & Testing Services Company of Daqing Oilfield Co. Ltd., Daqing 163000, China.

⁶ Center for High Pressure Science and Technology Advanced Research (HPSTAR), Changchun 130012, China.

temperature- and pressure-dependent physical properties of silicate melts is essential. In each stage of magmatism, the initial melt and the final intrusive or extrusive rock are not only affected by the physical and chemical evolution processes in the Earth and its interior, but they are also controlled by the density of the silicate melt. Therefore, the density crossover between the crystals and melt has a far-reaching impact on deep mantle melting and the existence of a magma ocean (Agee, 2008).

The upper mantle transition zone is considered to be a potentially water-rich reservoir, so the appropriate thermal anomaly process can quickly produce melts (Debayle et al., 2020; Pearson et al., 2014; Shao et al., 2021; Soltanmohammadi et al., 2018). Seismic wave research has shown that there is discontinuity at 410 km, and the D'' layer at the bottom of the lower mantle above the layer velocity will propagate abnormally, which is related to the existence of dense silicate melt in the lower mantle (Ohtani, 1983; Knittle & Jeanloz, 1991; Ohtani & Maeda, 2001; Sifré et al., 2014; Williams & Garnero, 1998). Mosenfelder et al. (2009) and Funamori and Sato (2010) proposed the possibility of density crossover in the deep mantle based on various mineral-physics data obtained by static-compression experiments. Shock-compression experiments have indicated that the density of melts does not exceed that of crystals with the same chemical composition in SiO₂ but does exceed in MgSiO₃ and Mg₂SiO₄ at the conditions of the deep mantle (Akins et al., 2004; Luo et al., 2004; Lyzenga et al., 1983; Miller et al., 1991; Mosenfelder et al., 2007). Therefore, different models of magma eruption and the magma ocean evolution of komatiite have been proposed (Inoue, 1994). Due to the phase transformation relationship under extremely high pressures and the uncertainty of the equation of state for silicate melt, it is difficult to make an objective evaluation of this hypothesis. The properties of silicate melts may have a significant impact on the chemical geodynamics of the upper mantle (Inoue, 1994; Matsukage et al., 2005; Romano, 2020). In addition, the seismic low-velocity zone (LVZ) of the upper mantle is generally associated with a low-viscosity asthenosphere that has a key role in decoupling tectonic plates from the mantle (Ricard et al., 1991). Experimental studies about the Earth

mantle conductivity have shown the importance of small amounts of hydrated CO₂-rich melts in the geophysical signature of the LVZ (Dasgupta et al., 2013; Gardésa et al., 2020; Hirschmann, 2010; Novella & Frost, 2014; Presnall & Gudfinnsson, 2005). The aforementioned geophysical and experimental geochemical studies strongly show that melt can exist in a deeper area in the Earth and its interior. Because the bulk elastic modulus of the silicate melt is much smaller than that of the surrounding minerals, the density of the silicate melt increases, becoming even higher than that of the surrounding minerals. Therefore, the properties of silicate melts are also one of the frontier issues in the study of the deep materials in the Earth (Matsukage et al., 2005; Mookherjee et al., 2008; Romano, 2020; Suzuki & Ohtani, 2003). The density plays a very important role in the chemical evolution of the Earth and other terrestrial planets.

For the range of upper mantle pressures, there are many experimental technical methods for the silicate melt density measurement, such as the Archimedes method under zero pressure and sound velocity measurements at zero pressure, the shock-compression method, the falling-sphere method, and the sink/float method (Agee, 1998; Funamori & Sato, 2010; Jing & Karato, 2008; Lange et al., 1987; Miller et al., 1991; Rivers & Carmichael, 1987; Stolper et al., 1981). The first two methods provide a basis for predicting the development of the quantitative volume model under atmospheric pressure and high temperatures, and the last two methods have been widely used to measure the densities of silicate melts under high pressures. However, there are many problems in these research methods, such as the quality of some thermodynamic parameters and input data involved in their calculation process and the scope of application of their own methods, which limit their application. In addition, in terms of the occurrence of a phase transition and the estimation of the melting temperature, the shock-compression method can solve some melt problems under deep mantle pressures, but the problem of crossover density of melts cannot be solved.

Another static compression technique, the sink/float method, can be determined directly without resorting to these indirect measurements of velocities.

It eliminates the need to measure the velocity of the sphere indirectly, overcomes the error caused by the velocity of the falling-sphere method. Therefore, the resulting error in the density should be potentially smaller, and the measurement error is reduced to 0.04 g cm⁻³ or 1% of the absolute density in the upper mantle pressure range (Jing & Karato, 2012). In this method, a limited number of minerals (e.g., feldspars, quartz; some garnets, spinels, olivines) that are suitable as possible candidates of buoyancy markers and a limited number of data points were obtained (Knoche & Luth, 1996). Moreover, mineral buoyancy markers have certain applicable systems and limitations. Chemical minerals as the candidates of buoyancy markers were chosen in the previous study: spinel (MgAl₂O₄, ρ_0 : 3.58 g cm⁻³), forsterite (Mg₂SiO₄, ρ_0 : 3.22 g cm⁻³), adularia (KAlSi₃O₈, ρ_0 : 2.56 g cm⁻³, and quartz (SiO₂, ρ_0 : g cm⁻³) (Knoche & Luth, 1996). Choosing a new stable buoyancy marker that can be used in different research systems is the key to the sink/float method. The accuracy of the melt density measurement depends on the resolution of the density difference of the buoyancy. The density range of the natural mineral density buoyancy marker is limited and often cannot meet the needs of practical research. To accurately measure the density of the melt, it is necessary to improve the resolution of the density difference of the buoyancy marker. Identifying a stable high-resolution density buoyancy marker for the sink/float method is urgently needed to obtain melt density measurements under high pressures. Using the Al₂O₃–Cr₂O₃ solid solution as a density buoyancy marker avoids the disadvantage of using natural minerals as a density buoyancy marker, and it has unique advantages. First, the density range of the materials in the mantle is 3.4–5.6 g/cm³ (Jordan, 1979), and the densities of Al₂O₃ and Cr₂O₃ are 3.9–4.0 g/cm³ and 5.21 g/cm³, respectively. A buoyancy marker with a density similar to that of silicate in the mantle can be obtained by preparing solid solutions with continuous changes in their components, which is more conducive to improving the resolution of the melt density. Second, the bulk elastic modulus of Al₂O₃ and Cr₂O₃, which are stable in the pressure and temperature range to be studied over the time scale of the experiment, are both > 200 GPa. Finally, the melting temperatures of

Al₂O₃ and Cr₂O₃ are higher than 2000 °C, and the chemical stability and hardness are very high. Thus, they can coexist with silicate under high-temperature and high-pressure conditions (Dorogokupets et al., 2016; Gasparik, 1984; Ringwood, 2012).

2. Experimental Methods

1. Synthesis experiment of Al₂O₃–Cr₂O₃ solid solution

Al₂O₃ and Cr₂O₃ powders with purity of 99.99% were mixed according to a stoichiometric ratio and were ground in an agate mortar for 2 h. Then, the mixture was placed in a muffle furnace at a temperature of 1200 °C for 10 h. After naturally cooling to room temperature, the samples were ground again for 2 h and then sintered at 1200 °C for 10 h. After all of these processes, the sintered powders were loaded into a rod balloon, and the hydrostatic pressure was increased to 70 MPa to prepare a cylindrical rod with a diameter of 6 mm and a length of 500 mm. Then, the rod was sintered in a vertical muffle furnace at a temperature of 1400 °C for 10 h to obtain a uniform cylindrical polycrystalline ceramic bar. Finally, the solid solutions were grown in a commercial optical floating zone furnace (CSI FZ-T-10000-H-VI-VP, Crystal Systems, Inc., Japan) which was equipped with four 1000 W halogen lamps as heat source. After optimization of the conditions, the optimum melt growth conditions were as follows: the feed and support rods were rotated in opposite directions at a rate of 5 rpm; the growth rate was 6 mm/h, the air flow rate was 0.5 L/min, and pressure of 0.2 MPa was maintained. The sample was heated in air at a rate of 1000 °C/h, after which the sample melting temperature was maintained for about 2 h, and the melting and solidification rate was set at 10 mm/h.

2. X-ray diffraction analysis of Al₂O₃–Cr₂O₃ solid solution

The samples and the raw materials were studied via X-ray diffraction (XRD) under ambient pressure and high pressure. First, the XRD patterns at ambient pressure were obtained using an X-ray diffractometer (Rigaku D/max 2550 VB ± 18 kW) using CuK α radiation ($\lambda = 1.5418 \text{ \AA}$), a graphite monochromator

with a step of 0.02° , a tube voltage of 50 kV, a tube current of 200 mA, and a scanning speed of $1^\circ/\text{min}$.

Second, several of the prepared samples (Al95Cr05, Al90Cr10, and Al30Cr70) were selected for high-pressure XRD analysis. The high-pressure experiments were carried out in a diamond anvil cell with a culet size of 500 μm . A steel T-301 was pre-indenting to 40 μm , and then a center hole with a diameter of 165 μm was drilled as the sample chamber. This chamber was filled with a small amount of sample and a tiny ruby chip. A 4:1 methanol-ethanol mixture was used as the pressure-transmitting medium, and the internal standard Au was used to measure the pressure (Anderson et al., 1989). The in situ high-pressure angle-dispersive synchrotron XRD experiments were carried out at the X17C beamline of the Brookhaven National Laboratory. A charge-coupled device (CCD) detector was used in the synchrotron radiation experiment, where an incident wavelength of the monochromatic beam of 0.4099 \AA and acquisition time of 600 s were used. All of the XRD patterns were integrated to obtain one-dimensional powder diffraction patterns using the FIT2D program, yielding patterns of one-dimensional intensity versus diffraction angle 2θ .

3. Results and discussion

1. X-ray diffraction under ambient pressure

A series of $\text{Al}_2\text{O}_3\text{-Cr}_2\text{O}_3$ solid solutions were prepared to obtain buoyancy markers with continuous density changes. The XRD patterns of the relevant samples and raw materials are shown in Fig. 1, and all of the compositions form substitutional solid solutions with a high crystallinity. The shapes of all of the XRD patterns are similar; however, the positions of the diffraction peaks are slightly shifted toward a smaller angle as the Cr^{3+} content increases. This can be explained by the replacement of larger Cr^{3+} (0.62 \AA) ions with smaller Al^{3+} (0.53 \AA) ions (Nguyen et al., 2019).

Then, the lattice parameters of the samples were calculated using the Rietveld method to refine their structures, and the refined results are shown in Table 1 (Barsoum, 1997; Gehre et al., 2015; Graham, 1960; Li et al., 2013; Murakami et al., 2002).

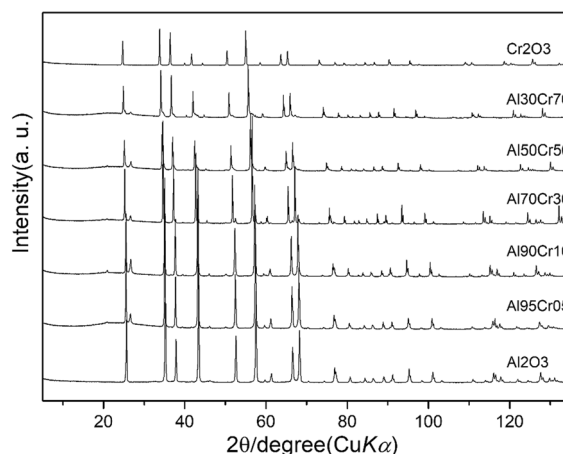


Figure 1
X-ray diffraction patterns of the prepared $\text{Al}_2\text{O}_3\text{-Cr}_2\text{O}_3$ solid solutions under ambient pressure

Table 1

The fitted cell parameters of the prepared $\text{Al}_2\text{O}_3\text{-Cr}_2\text{O}_3$ solid solutions

Cr content (molar percentage)	a (\AA)	c (\AA)
0	4.7537(41)	12.9888(15)
5	4.7597(35)	13.0261(93)
10	4.7679(93)	13.0620(09)
30	4.8095(84)	13.1647(64)
50	4.8483(28)	13.2738(72)
70	4.8945(78)	13.3799(54)
100	4.9598(46)	13.6007(57)

Figure 2 shows the lattice parameters a and c both changed linearly with the Cr_2O_3 content. The results of the linear fitting are shown in Eqs. (1) and (2):

$$a = 4.7490(3) + 0.2077(5)\chi \quad (1)$$

$$c = 12.9911(5) + 0.5879(5)\chi, \quad (2)$$

where χ is the mole percent content of Cr_2O_3 in the $\text{Al}_2\text{O}_3\text{-Cr}_2\text{O}_3$ solid solution. The doping of Cr^{3+} ions causes the $\alpha\text{-Al}_2\text{O}_3$ to produce a large lattice strain in the c axial direction [the slope of a is 0.2077(5), and the slope of c is 0.5879(5)], and this may be related to the crystalline structure of $\alpha\text{-Al}_2\text{O}_3$. In their structures, which belong to space group $R\bar{3}c$, the oxygen atoms are arranged in the densest hexagonal packing pattern, while the Al/Cr atoms fill the 2/3 octahedral interstices, and a single cell contains 12 Al/Cr and 18

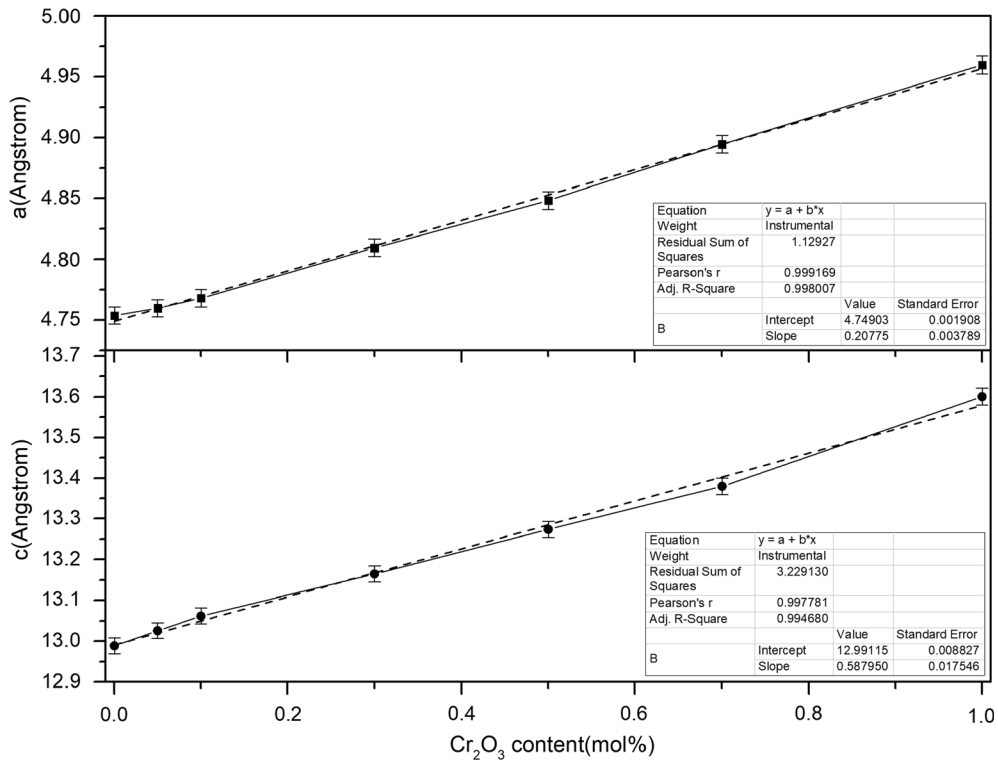


Figure 2

The change curve of the unit cell parameters of the prepared Al₂O₃-Cr₂O₃ solid solutions with different Cr₂O₃ contents

O atoms (Khatibi, 2011). Due to the doping of larger Cr³⁺ ions, one third of the interstices are empty in the *a(b)* axis direction. The existence of these vacancies releases the lattice strain caused by the Cr³⁺ ion doping. Although the lattice parameters gradually increase with the increasing Cr³⁺ concentration, the expansion and contraction of the atomic radii of Cr³⁺ and Al³⁺, respectively, are equal in magnitude. Therefore, Vegard's law holds true here, and the obtained fitting results follow it (Kirkaldy, 2007; Zhang and Li, 2014).

Although Al₂O₃-Cr₂O₃ solid solutions with obvious changes in lattice parameters have been seen, the content and form of the Cr₂O₃ still need to be considered further because in the Al-Cr-O system, Cr₂O₃ exists in two indistinguishable and separate forms (i.e., the free form and dissolved form) in the solid solution (Nguyen et al., 2021; Zhao et al., 2018). However, if the relationship between the diffraction angle (2θ) and the Cr₂O₃ content (χ , in mol%) of the diffraction peak is determined, the

Cr₂O₃ content of the Al₂O₃-Cr₂O₃ solid solution can be calculated according to the diffraction angle of the (104) plane. Therefore, in view of the above two factors, the Cr₂O₃ content is obtained by the classical Bragg's law.

Figure 3 shows the diffraction peak of (104) shifts toward the lower angles. There should be a functional relationship between the diffraction angles corresponding to the (104) plane and the amount of Cr₂O₃ in the solid solution. The relationship between the diffraction angle of the (104) plane and the lattice parameters should be given by Eq. (3) based on the formula for the lattice spacing of a hexagonal cell and Bragg's law.

$$2\theta = 2 \arcsin \left(\frac{\lambda}{2a} \sqrt{\frac{4}{3}(h^2 + hk^2 + k^2) + \left(\frac{a}{c}\right)^2 l^2} \right), \quad (3)$$

where λ is the wavelength of the incident radiation (Cu: 1.5418 Å), a and c are the lattice parameters,

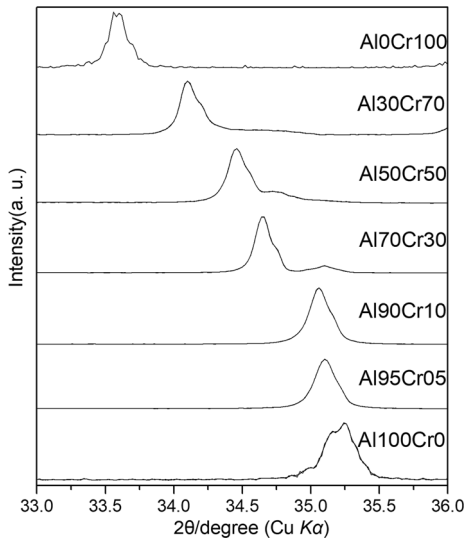


Figure 3
Enlarged X-ray diffraction patterns of the (104) plane

and h , k , and l are the crystallographic indices. Then, by substituting lattice parameters a and c from Eqs. (1) and (2) into Eq. (3), the relationship between the diffraction angle of the (104) plane and the Cr_2O_3 content can be obtained. However, this relationship is an inverse trigonometric function, which is very difficult to calculate. To simplify the calculation, different Cr_2O_3 contents were substituted into Eq. (3) to determine the corresponding diffraction angles,

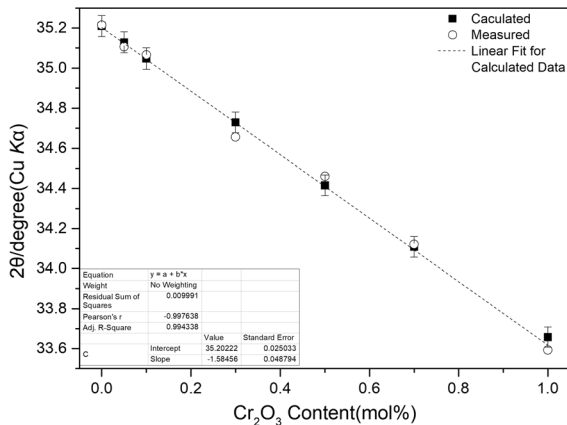


Figure 4
The relationship between the diffraction angle of the (104) plane and the Cr_2O_3 content. The black squares and the hollow circles represent the calculated values and the measured values, respectively. The dotted line represents the linear fitting of the intercept and slope

and then the relationship diagram of the two variables was obtained (as seen in Fig. 4).

The results indicate that the Cr_2O_3 content and the diffraction angle exhibit a linear relationship that can be fitted using Eq. (4), and the theoretical calculation results are in good agreement with the experimental data. Therefore, the Cr_2O_3 contents of the Al_2O_3 – Cr_2O_3 solid solutions can be determined based on the diffraction angle 2θ .

$$\chi = 22.2157(69) - \frac{2\theta}{1.5845(6)}. \quad (4)$$

Although the Cr_2O_3 content in the Al_2O_3 – Cr_2O_3 solid solutions has been clarified, their densities, which are the fundamental problem in using them as a buoyancy marker, are still not solved. The theoretical density of a material is an intrinsic property, but it is difficult to measure. However, the true density of a material can be measured and can reflect its theoretical density. Therefore, to utilize the Al_2O_3 – Cr_2O_3 solid solution as a buoyancy marker in the sink/float method, it is necessary to determine either its theoretical density or its true density.

As is well known, the density of a material is defined as the ratio of the sample mass to the volume occupied by that mass. Thus, the theoretical density (ρ) of the Al_2O_3 – Cr_2O_3 solid solution can be simply calculated as follows:

$$\rho = \frac{M}{V}, \quad (5)$$

where M and V are the mass and volume of the unit cell, respectively. However, for a hexagonal cell of Al – Cr – O , each cell has six units. Therefore, Eq. (5) can be rewritten as

$$\rho = \frac{M}{V} = \frac{4\sqrt{3}[m_{\text{Al}_2\text{O}_3} \times (1 - \chi) + m_{\text{Cr}_2\text{O}_3} \times \chi]}{N_A a^2 c}, \quad (6)$$

where $m_{\text{Al}_2\text{O}_3}$ and $m_{\text{Cr}_2\text{O}_3}$ are the molecular weights of Al_2O_3 and Cr_2O_3 , respectively, and N_A is Avogadro's number.

The theoretical density of the Al_2O_3 – Cr_2O_3 solid solution (ρ) was obtained by substituting different contents of Cr_2O_3 . The fitting calculation in Fig. 5 indicates that there is a second-order polynomial relationship between the theoretical density and the Cr_2O_3 content (as shown in

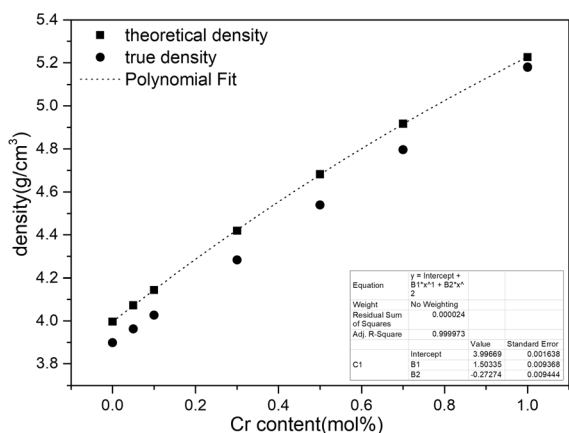


Figure 5

Relationship between the density and Cr₂O₃ content. The squares and the circles represent the theoretical density and true density, respectively. The dotted line represents the linear fitting of the intercept and slope

Eq. (7)). However, the actual density is lower than the theoretical density, which may be due to the different densities and microstructures of the solid solutions caused by the preparation method, as well as the crystal defects in the solid solutions, the existence of impurities, and experimental errors. In a previous study of the effect of TiO₂ on the densification behavior and properties on alumina chromium ceramics, Nath et al. (2013) found that the density of the sample was the highest at 1650 °C. Therefore, the true density of the Al–Cr solid solution measured by Nath et al. was 4.50 g/cm³, which is consistent with the 4.53 g/cm³ obtained in this study.

$$\rho = -0.2727(4) \times \chi^2 + 1.5033(5) \times \chi + 3.9966(9). \quad (7)$$

2. X-ray diffraction under high pressure

Although buoyancy markers with different densities were obtained by changing the content of Cr₂O₃ in the Al₂O₃–Cr₂O₃ solid solutions under ambient pressure, the compressibility of these solid solutions needed to be studied further. The XRD experiments under high pressure were performed using XRD characterization under high synchrotron radiation pressures. Then, the bulk elastic moduli of the Al₂O₃–Cr₂O₃ solid solutions and their unit cell volumes under different pressures were obtained, providing an experimental basis for calculating the

density of a buoyancy marker under different pressures. Based on the XRD results under ambient pressure, several Al₂O₃–Cr₂O₃ solid solutions (Al95Cr05, Al90Cr10, and Al30Cr70) were selected for the XRD characterization under high synchrotron radiation, and their elastic properties were calculated by using the third-order Birch–Murnaghan equation of state (EOS).

The crystal structure of Al30Cr70 is still consistent with that of Al₂O₃, and the cell parameters of the sample under high pressure were refined by PowderCell software (Nolze & Kraus, 1998). As shown in Fig. 6a, b, cell parameters *a* and *c* gradually decreased with the increasing pressure. From the variation curve of *a* with pressure (Fig. 6c), it can be seen that the bulk elastic modulus of Al30Cr70 is 284.40 GPa, which is slightly higher than that of Al₂O₃ based on fitting the pressure and cell volume curve (as shown in Fig. 6d).

The XRD results for sample Al90Cr10 show that cell parameters *a* and *c* also decreased with the increasing pressure (Fig. 7a, b). As can be seen from Fig. 7d, the bulk elastic modulus of sample Al90Cr10 is 207.89 GPa.

Similarly, the XRD results for sample Al95Cr05 show that cell parameters *a* and *c* also decreased with the increasing pressure (Fig. 8a, b). It can be concluded from Fig. 8d that the bulk elastic modulus of sample Al95Cr05 is 249.30 GPa.

A substance with a larger ion will have a smaller bulk elastic modulus than a substance with a smaller ion. Based on the XRD analysis under high pressure, we conclude that the higher the Cr₂O₃ content of the Al₂O₃–Cr₂O₃ solid solution, the smaller the bulk elastic modulus. Previous studies on elastic properties of Al₂O₃ and Cr₂O₃ showed that the bulk elastic modulus of Al₂O₃ and Cr₂O₃ is 254.25 GPa and 240.00 GPa, respectively (Rekhi, et al., 2000; Ru & Qiu, 2009). Al95Cr05 is closer to the raw material (Al₂O₃) than Al90Cr10 in terms of chemical composition. Thus, in this study, the bulk elastic modulus of Al95Cr05 is slightly smaller than that of Al₂O₃, but significantly larger than that of Al90Cr10. In terms of the stoichiometric ratio, Al95Cr05 is closer to the raw material (Al₂O₃) than Al90Cr10, and its bulk elastic modulus is significantly greater than that of

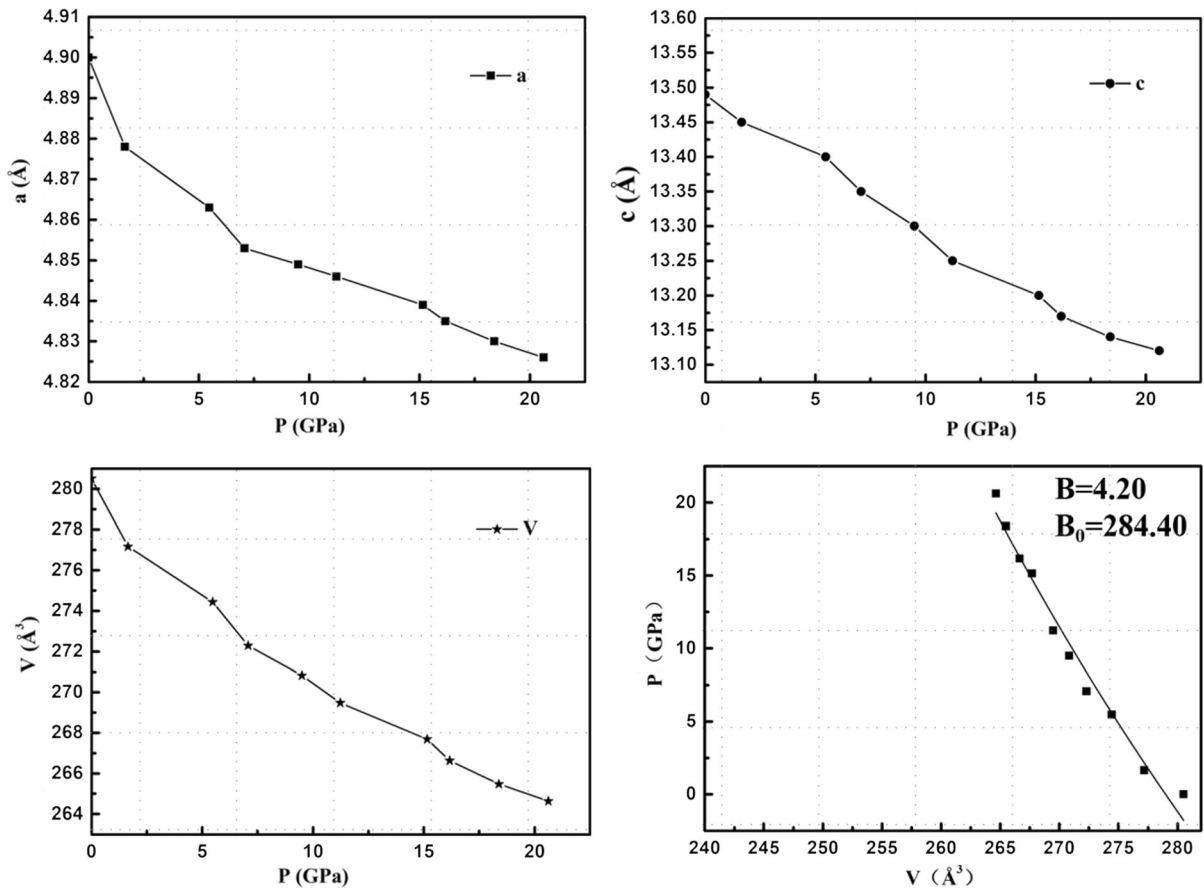


Figure 6

The variations in the cell parameters of sample Al₃₀Cr₇₀ with pressure. **a–c** Variations in cell parameters a and c and the volume V with pressure, respectively. **d** Fitting curve of the change in volume with pressure

sample Al₉₀Cr₁₀, but the bulk elastic modulus of Al₃₀Cr₇₀ is significantly larger than that of the previous two samples. We hypothesize that there are two possible reasons for this result. First, the introduction of a small amount of Cr₂O₃ leads to the larger Cr³⁺ disorderly occupying the lattice site of the hexagonal structure, so this structure is easily deformed under high pressures compared with the original structure, which makes the structure of the Al₂O₃–Cr₂O₃ solid solution easier to compress. When the Cr₂O₃ content reaches a certain proportion, the orderly introduction of Cr₂O₃ produces a more compact structure, resulting in an increase in the bulk elastic modulus. Second, the Cr₂O₃ content of Al₃₀Cr₇₀ is large, and the miscibility of the Al₂O₃–Cr₂O₃ solid solution is poor,

which may lead to the precipitation of more Cr₂O₃ in the sample. Thus, the bulk elastic modulus of Al₃₀Cr₇₀ under high pressures is significantly higher than those of Al₉₅Cr₀₅ and Al₉₀Cr₁₀. However, a more specific reason still needs to be obtained through additional experiments and theoretical calculations in future research.

4. Conclusions

In summary, the Al₂O₃–Cr₂O₃ solid solution, which can be used as a buoyancy marker in the future, was prepared using the optical floating zone melting method, and this solid solution makes up for the lack of resolution of natural minerals as buoyancy

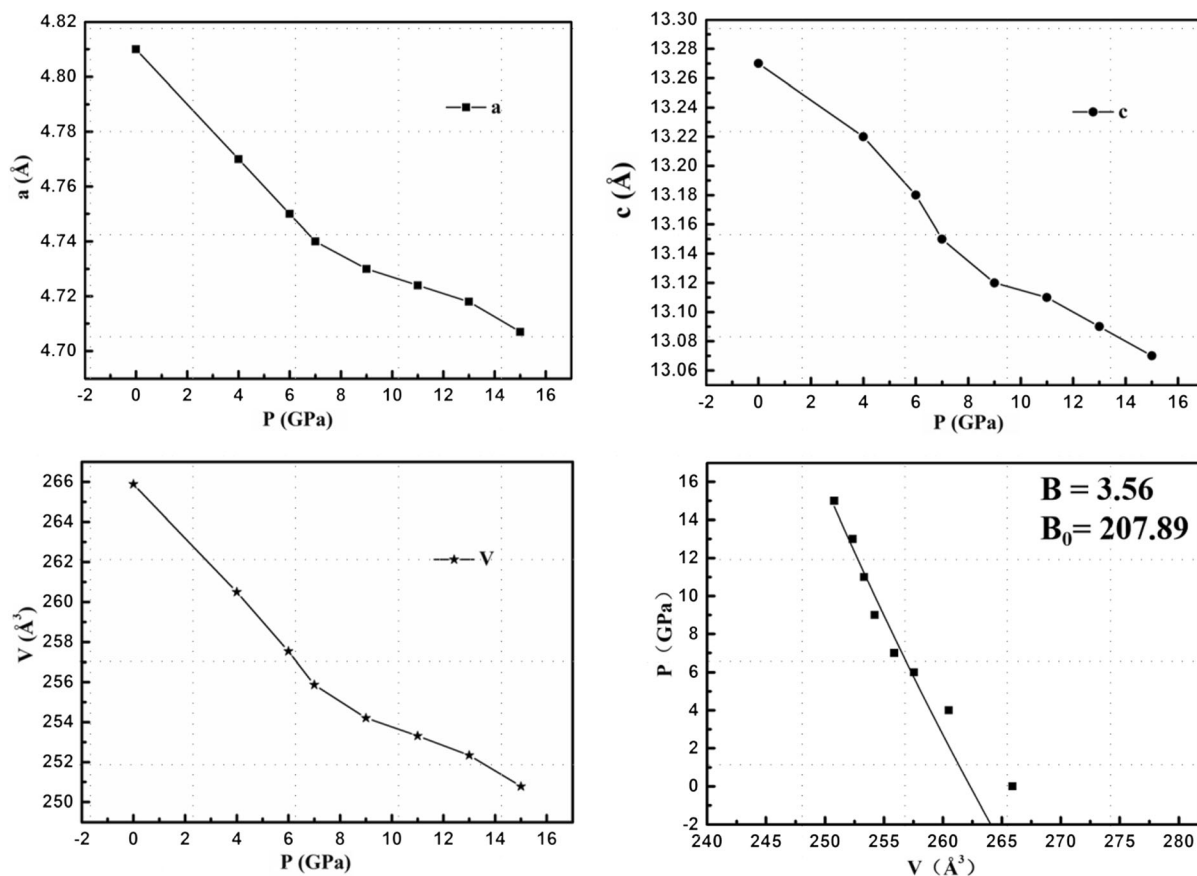


Figure 7

Variations in the cell parameters of sample Al₉₀Cr₁₀ with pressure. **a–c** Variations in cell parameters a and c and the volume V with pressure, respectively. **d** Fitting curve of the change in volume with pressure

markers. The crystalline structures of the Al₂O₃-Cr₂O₃ solid solutions were characterized via XRD at ambient pressure. The results show that lattice parameters a and c increase with the increasing Cr₂O₃ content. However, due to the doping of Cr³⁺ ions, the lattice strain in the c -axis direction is more serious. The angles of the diffraction peak decrease linearly with increasing Cr₂O₃ content. In addition, it was found that the relationship between the theoretical density and the Cr₂O₃ content can be fitted using a second-order polynomial. Furthermore, in order to study the stability and compressibility of Al₂O₃-Cr₂O₃ solid solutions under high pressure, Al₉₅Cr₀₅, Al₉₀Cr₁₀, and Al₃₀Cr₇₀ were analyzed via the synchrotron radiation XRD analysis under different pressures. The results show that the cell parameters of the three solid solutions vary with pressure. In

addition, the bulk elastic moduli of these three solid solutions were obtained, providing experimental data for the design and preparation of different buoyancy markers in the future.

Acknowledgements

The authors are grateful to the anonymous reviewers for their incisive reviews of the manuscript. This research was supported by the National Youth Sciences Foundation of China (No. 41502044).

Declarations

Conflicts of interest The authors declare no conflict of interest.

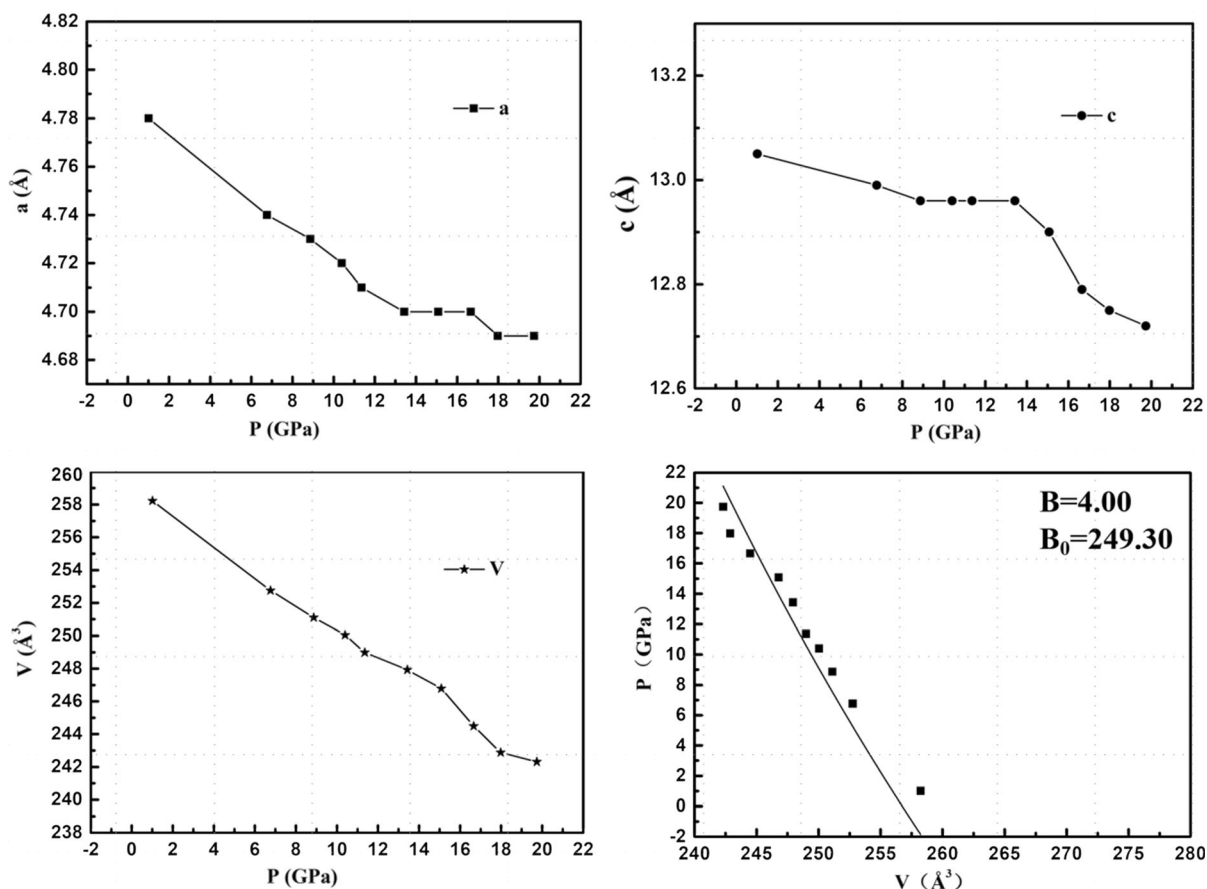


Figure 8

Variations in the cell parameters of sample A195Cr05 with pressure. **a–c** Variations in cell parameters a and c and the volume V with pressure, respectively. **d** Fitting curve of the change in volume with pressure

Publisher's Note Springer Nature remains neutral with regard to jurisdictional claims in published maps and institutional affiliations.

REFERENCES

- Agee, C. B. (1998). Crystal-liquid density inversions in terrestrial and lunar magmas. *Earth and Planetary Science Letters*, *107*, 63–74. [https://doi.org/10.1016/S0031-9201\(97\)00124-6](https://doi.org/10.1016/S0031-9201(97)00124-6)
- Agee, C. B. (2008). Static compression of hydrous silicate melt and the effect of water on planetary differentiation. *Earth and Planetary Science Letters*, *265*, 641–654. <https://doi.org/10.1016/j.epsl.2007.11.010>
- Akins, J. A., Luo, S. N., Asimow, P. D., & Ahrens, T. J. (2004). Shock-induced melting of MgSiO₃ perovskite and implications for melts in Earth's lowermost mantle. *Geophysical Research Letters*, *31*, L14612. <https://doi.org/10.1029/2004GL020237>
- Anderson, O. L., Isaak, D. G., & Yamamoto, S. (1989). Anharmonicity and the equation of state for gold. *Journal of Applied Physics*, *65*, 1534–1539. <https://doi.org/10.1063/1.342969>
- Barsoum, M. W. (1997). *Fundamentals of ceramics* (1st ed., p. P66). McGraw-Hill.
- Bouhifd, M. A., Clesi, V., Boujibar, A., Bolfan-Casanovaa, N., Cartierc, C., Hammoudaa, T., Boyeta, M., Manthilakea, G., Monteuxa, J., & Andrault, D. (2016). Silicate melts during Earth's core formation. *Chemical Geology*, *461*, 128–139. <https://doi.org/10.1016/j.chemgeo.2016.12.035>
- Chabot, N. L., Draper, D. S., & Agee, C. B. (2005). Conditions of core formation in the earth: Constraints from Nickel and Cobalt partitioning. *Geochimica Et Cosmochimica Acta*, *69*(8), 2141–2151. <https://doi.org/10.1016/j.gca.2004.10.019>
- Courtial, P., Ohtani, E., & Dingwell, D. B. (1997). High-temperature densities of some mantle melts. *Geochimica Et Cosmochimica Acta*, *61*(15), 3111–3119. [https://doi.org/10.1016/S0016-7037\(97\)00154-3](https://doi.org/10.1016/S0016-7037(97)00154-3)
- Dasgupta, R., Mallik, A., Tsuno, K., Withers, A. C., Hirth, G., & Hirschmann, M. M. (2013). Carbon-dioxide-rich silicate melt in

- the Earth's upper mantle. *Nature*, 493, 211–215. <https://doi.org/10.1038/nature11731>
- Debayle, E., Bodin, T., Durand, S., & Ricard, Y. (2020). Seismic evidence for partial melt below tectonic plates. *Nature*, 586(7830), 555–559. <https://doi.org/10.1038/s41586-020-2809-4>
- Dorogokupets, P. I., Sokolova, T. S., Dymshits, A. M., & Litasov, K. D. (2016). Thermodynamic properties of rock-forming oxides, α -Al₂O₃, Cr₂O₃, α -Fe₂O₃, and Fe₃O₄ at high temperatures and pressures. *Geodynamics & Tectonophysics*, 7(3), 459–476. <https://doi.org/10.5800/GT-2016-7-3-0217>
- Eakins-Tanton, L. T. (2012). Magma oceans in the inner solar system. *Annual Review of Earth and Planetary Sciences*, 40, 113–139. <https://doi.org/10.1146/annurev-earth-042711-105503>
- Funamori, N., & Sato, T. (2010). Density contrast between silicate melts and crystals in the deep mantle: An integrated view based on static-compression data. *Earth and Planetary Science Letters*, 295, 435–440. <https://doi.org/10.1016/j.epsl.2010.04.021>
- Gardésa, E., Laumonier, M., Massuyeau, M., & Gaillard, F. (2020). Unravelling partial melt distribution in the oceanic low velocity zone. *Earth and Planetary Science Letters*, 540(15), 116242. <https://doi.org/10.1016/j.epsl.2020.116242>
- Gasparik, T. (1984). Experimentally determined stability of clinopyroxene + garnet + corundum in the system CaO-MgO-Al₂O₃-SiO₂. *American Mineralogist*, 69, 1025–1035.
- Gehre, P., Aneziris, C. G., & Parr, C. (2015). Self-glazing SiC-andalusite refractories for high temperature gasification applications. *European Ceramic Society*, 35, 1613–1620.
- Graham, J. C. D. (1960). Temperature dependence of anisotropy and saturation magnetization in iron and iron-silicon alloys. *Journal of Physics and Chemistry of Solids*, 31(5), 18–25. <https://doi.org/10.1063/1.1984640>
- Guillaume, F., Yoshio, K., & Chrystèle, S. (2018). Melting in the Earth's Deep Interior. *Elsevier*, 4, 115–134. <https://doi.org/10.1016/B978-0-12-811301-1.00004-6>
- Hirschmann, M. M. (2010). Partial melt in the oceanic low velocity zone. *Physics of the Earth and Planetary Interiors*, 179(1–2), 60–71. <https://doi.org/10.1016/j.pepi.2009.12.003>
- Inoue, T. (1994). Effect of water on melting phase relations and melt composition in the system Mg₂SiO₄-MgSiO₃-H₂O up to 15 GPa. *Physics of the Earth and Planetary Interiors*, 85, 237–263. [https://doi.org/10.1016/0031-9201\(94\)90116-3](https://doi.org/10.1016/0031-9201(94)90116-3)
- Jing, Z., & Karato, S. (2008). Compositional effect on the pressure derivatives of bulk modulus of silicate melts. *Science Letters*, 272, 429–436. <https://doi.org/10.1016/j.epsl.2008.05.013>
- Jing, Z., & Karato, S. (2012). Effect of H₂O on the density of silicate melts at high pressures: Static experiments and the application of a modified hard-sphere model of equation of state. *Geochimica Et Cosmochimica Acta*, 85, 357–372. <https://doi.org/10.1016/j.gca.2012.03.001>
- Jordan, T. H. (1979). Structural geology of the Earth's interior. *Proceedings of the National Academy of Sciences of the United States of America*, 76(9), 4192–4200. <https://doi.org/10.1073/pnas.76.9.4192>
- Khatibi, A. (2011). Deposition and phase transformations of ternary Al-Cr-O thin films. *Linköping Studies in Science and Technology, Licentiate Thesis No. 1474*.
- Kirkaldy, J. S. (2007). Flux-independent theory of nonlinear diffusion for Vegard's law solutions. *Materials Science and Engineering*, 444, 104–111. <https://doi.org/10.1016/j.msea.2006.08.073>
- Knittle, E., & Jeanloz, R. (1991). Earth's core-mantle boundary: Results of experiments at high pressures and temperatures. *Science*, 22, 1438–1443. <https://doi.org/10.1126/science.251.5000.1438>
- Knoche, R., & Luth, R. W. (1996). Density measurements on melts at high pressure using the sink/float method: Limitations and possibilities. *Chemical Geology*. [https://doi.org/10.1016/0009-2541\(95\)00176-x](https://doi.org/10.1016/0009-2541(95)00176-x)
- Kuwahara, H., Gotou, H., Shinmei, T., Ogawa, N., Yamaguchi, A., Takahata, N., Sano, Y., Yagi, T., & Sugita, S. (2017). High pressure experiments on metal-silicate partitioning of chlorine in a Magma Ocean: Implications for terrestrial chlorine depletion. *Geochemistry, Geophysics, Geosystems*, 18, 3929–3945. <https://doi.org/10.1002/2017GC007159>
- Lagos, M., Ballhaus, C., Münker, C., Wohlgemuth-Ueberwasser, C., Berndt, J., & Kuzmin, D. V. (2008). The Earth's missing lead may not be in the core. *Nature*, 456, 89–92. <https://doi.org/10.1038/nature07375>
- Lange, R. A., & Carmichael, I. S. E. (1987). Densities of Na₂O-K₂O-CaO-MgO-FeO-Fe₂O₃-Al₂O₃-TiO₂-SiO₂ liquids: New measurements and derived partial molar properties. *Geochimica Et Cosmochimica Acta*, 51, 2931–2946. [https://doi.org/10.1016/0016-7037\(87\)90368-1](https://doi.org/10.1016/0016-7037(87)90368-1)
- Li, J., & Agee, C. B. (2001). The effect of pressure, temperature, oxygen fugacity and composition on partitioning of nickel and cobalt between liquid Fe-Ni-S alloy and liquid silicate Implications for the Earth's core formation. *Geochimica Et Cosmochimica Acta*, 65, 1821–1832.
- Li, Y. Q., Ke, C. M., Gao, S., Zhang, Y. F., Zhao, J. Z., & Ye, G. T. (2013). Effects of zirconia on the thermal shock resistance of high chrome refractories for coal slurry gasifier. Proceedings UNITECR (2013), *British Columbia, Canada*, pp. 1127–1132. <https://doi.org/10.1002/9781118837009.ch208>
- Luo, S. N., Akins, J. A., Ahrens, T. J., & Asimow, P. D. (2004). Shock-compressed MgSiO₃ glass, enstatite, olivine, and quartz: opticaemission, temperatures, and melting. *Journal of Geophysical Research*, 109, B05205. <https://doi.org/10.1029/2003JB002860>
- Lyzenga, G. A., Ahrens, T. J., & Mitchell, A. C. (1983). Shock temperatures of SiO₂ and their geophysical implications. *Journal of Geophysical Research*, 88, 2431–2444. <https://doi.org/10.1029/JB088iB03p02431>
- Matsukage, K. N., Jing, Z. C., & Karato, S. (2005). Density of hydrous silicate melt at the conditions of Earth's deep upper mantle. *Nature*, 438, 488–491. <https://doi.org/10.1038/nature04241>
- Miller, G. H., Stolper, E. M., & Ahrens, T. J. (1991). The equation of state of a molten komatiite. Shock wave compression to 36 GPa. *Journal of Geophysical Research*, 96, 11831–11848. <https://doi.org/10.1029/91JB01204>
- Mookherjee, M., Stixrude, L., & Karki, B. (2008). Hydrous silicate melt at high pressure. *Nature*, 452, 983–986. <https://doi.org/10.1038/nature06918>
- Mosenfelder, J. L., Asimow, P. D., & Ahrens, T. J. (2007). Thermodynamic properties of Mg₂SiO₄ liquid at ultra-high pressures from shock measurements to 200 GPa on forsterite and wadsleyite. *Journal of Geophysical Research*, 112, B06208. <https://doi.org/10.1029/2006JB004364>
- Mosenfelder, J. L., Asimow, P. D., Frost, D. J., Rubie, D. C., & Ahrens, T. J. (2009). The MgSiO₃ system at high pressure: thermodynamic properties of perovskite, postperovskite, and

- melt from global inversion of shock and static compression data. *Journal of Geophysical Research*, 114, B01203. <https://doi.org/10.1029/2008JB005900>
- Murakami, Y., Hirata, T., & Tsuru, Y. (2002). Metastable phase relationship in the $\text{Al}_2\text{O}_3\text{-Cr}_2\text{O}_3$ system and phase equilibria of 1:1 composition at 1200 °C. *Journal of the Ceramic Society of Japan*, 110, 541–543. <https://doi.org/10.2109/jcersj.110.541>
- Mysen, B. (2018). Mass transfer in the Earth's interior: Fluid-melt interaction in aluminosilicate-C-O-H-N systems at high pressure and temperature under oxidizing conditions. *Progress in Earth and Planetary Science*, 5(6), 1–18. <https://doi.org/10.1186/s40645-017-0161-6>
- Nath, M., Sen, S., Banerjee, K., Ghosh, A., & Tripathi, H. S. (2013). Densification behavior and properties of alumina-chrome ceramics: Effect of TiO_2 . *Ceramics International*, 39(1), 227–232. <https://doi.org/10.1016/J.CERAMINT.2012.06.013>
- Nguyen, D. K., Bach, Q. V., Kim, B., Lee, H., Kang, C., & Kim, I. T. (2019). Synthesis of Cr-doped Al_2O_3 by Pechini sol-gel method and its application for reversible thermochromic sensors. *Materials Chemistry and Physics*, 223, 708–714. <https://doi.org/10.1016/j.matchemphys.2018.11.070>
- Nguyen, V. Q., Nguyen, T. H., Tu, N., Trung, D. Q., Anh, D. D., Tran, M. T., Hung, N. D., Viet, D. X., & Huy, P. T. (2021). A high quantum efficiency plant growth LED by using a deep-red-emitting $\alpha\text{-Al}_2\text{O}_3\text{:Cr}^{3+}$ phosphor. *Dalton Transactions*, 50, 12570–12582. <https://doi.org/10.1039/d1dt00115a>
- Nolze, G., & Kraus, W. (1998). Powder diffraction. *Journal of Applied Crystallography*, 13(4), 256–259.
- Novella, D., & Frost, D. J. (2014). The composition of hydrous partial melts of garnet peridotite at 6 GPa: Implications for the origin of Group II Kimberlites. *Journal of Petrology*, 55(11), 2097–2124. <https://doi.org/10.1093/ptrology/egu051>
- Ohtani, E. (1983). Melting temperature distribution and fractionation in the lower mantle. *Physics of the Earth and Planetary Interiors*, 33(1), 12–25. [https://doi.org/10.1016/0031-9201\(83\)90003-1](https://doi.org/10.1016/0031-9201(83)90003-1)
- Ohtani, E., & Maeda, M. (2001). Density of basaltic melt at high pressure and stability of the melt at the base of the lower mantle. *Earth and Planetary Science Letters*, 193(1–2), 69–75. [https://doi.org/10.1016/S0012-821X\(01\)00505-2](https://doi.org/10.1016/S0012-821X(01)00505-2)
- Pearson, D. G., Brenker, F. E., Nestola, F., McNeill, J., Nasdala, L., Hutchison, M. T., Matveev, S., Mather, K., Silversmit, G., Schmitz, S., Vekemans, B., & Vincze, L. (2014). Hydrous mantle transition zone indicated by ringwoodite included within diamond. *Nature*, 507, 221–224. <https://doi.org/10.1038/nature13080>
- Presnall, D. C., & Gudfinnsson, G. H., (2005). Carbonate-rich melts in the oceanic low-velocity zone and deep mantle. In G. R. Foulger, J. H. Natland, D. C. Presnall, & D. L. Anderson (Eds.), *Plates, plumes, and paradigms: Geological Society of America Special Paper* 388 (pp. 207–216). <https://doi.org/10.1130/0-8137-2388-4.207>.
- Rekhi, S., Dubrovinsky, L. S., Ahuja, R., Saxena, S. K., & Johansson, B. (2000). Experimental and theoretical investigations on eskolaite (Cr_2O_3) at high pressures. *Journal of Alloys and Compounds*, 302(1), 16–20.
- Ricard, Y., Doglioni, C., & Sabadini, R. (1991). Differential rotation between lithosphere and mantle: A consequence of lateral mantle viscosity variations. *Journal of Geophysical Research*, 96, 8407–8415. <https://doi.org/10.1029/91JB00204>
- Ringwood, A. E. (2012). Mineralogical constitution of the deep mantle. *Journal of Geophysical Research*, 67(10), 4005–4010. <https://doi.org/10.1029/JZ067i010p04005>
- Rivers, M. L., & Carmichael, I. S. E. (1987). Ultrasonic studies of silicate melts. *Journal of Geophysical Research*, 92, 9247–9270. <https://doi.org/10.1029/JB092iB09p09247>
- Romano, C. (2020). Editorial for the special issue properties of melt and minerals at high pressures and high temperature. *Minerals*, 10(8), 723–729. <https://doi.org/10.3390/min10080723>
- Ru, Q., & Qiu, X. L. (2009). The electronic structure and mechanical property of $\alpha\text{-Al}_2\text{O}_3$ by first principles calculation. *Materials Research and Application*, 3(3), 162–167.
- Shao, J., Xu, H. H., Zhan, Y. Q., Shi, X. B., & Wang, X. F. (2021). The effect of water content in the Upper Mantle on the Oceanic crustal thickness during seafloor spreading: Numerical modeling. *Earth Science*, 46(3), 826–839. <https://doi.org/10.3799/dqkx.2020.336>
- Sifré, D., Gardés, E., Massuyeau, M., Hashim, L., Hier-Majumder, S., & Gaillard, F. (2014). The electrical conductivity during incipient melting in the oceanic low-velocity zone. *Nature*, 509, 81–85. <https://doi.org/10.1038/nature13245>.
- Solomatova, N. V., & Caracas, R. (2021). Buoyancy and structure of volatile-rich silicate melts. *Journal of Geophysical Research*, 126(2), 45–59. <https://doi.org/10.1029/2020JB021045>
- Soltanmohammadi, A., Grégoire, M., Rabinowicz, M., Gerbault, M., Ceuleneer, G., Rahgoshay, M., Bystricky, M., & Benoit, M. (2018). Transport of volatile-rich melt from the mantle transition zone via compaction pockets: Implications for mantle metasomatism and the origin of alkaline lavas in the Turkish-Iranian Plateau. *Journal of Petrology*, 59(12), 2273–2310. <https://doi.org/10.1093/ptrology/egy097>
- Stolper, E., Walker, D., Hager, B. H., & Hays, J. F. (1981). Melt segregation from partially molten source regions: The importance of melt density and source region size. *Journal of Geophysical Research*, 86, 6261–6271. <https://doi.org/10.1029/JB086iB07p06261>
- Suzuki, A., & Ohtani, E. (2003). Density of peridotite melts at high pressure. *Physics and Chemistry of Minerals*, 30(8), 449–456. <https://doi.org/10.1007/s00269-003-0322-6>
- Williams, Q., & Garnero, E. J. (1998). Seismic evidence for partial melt at the base of the Earth's mantle. *Science*, 273, 1528–1530. <https://doi.org/10.1126/science.273.5281.1528>
- Zhang, L., & Li, S. C. (2014). Empirical atom model of Vegard's law. *Physica B: Condensed Matter*, 434, 38–43. <https://doi.org/10.1016/j.physb.2013.10.066>
- Zhao, P. D., Zhao, H. Z., Yu, J., Zhang, H., Gao, H. J., & Chen, Q. (2018). Crystal structure and properties of $\text{Al}_2\text{O}_3\text{-Cr}_2\text{O}_3$ solid solutions with different Cr_2O_3 contents. *Ceramics International*, 44, 1356–1361. <https://doi.org/10.1016/j.ceramint.2017.08.195>